Available online at www.sciencedirect.com
SCIENCE DIRECT
Journal of Nuclear Materials 354 (2006) 14–27
journal of nuclear materials
www.elsevier.com/locate/jnucmat

An experimental study of the dissolution rates of Nd-britholite, an apatite-structured actinide-bearing waste storage host analogue

Claire Chaïrat [a,b], Eric H. Oelkers [a,*], Jacques Schott [a], Jean-Eric Lartigue [b]

[a] Géochimie et Biogéochimie Expérimentale, LMTG, CNRS/Université Paul Sabatier, 14 rue Edouard Belin, 31400 Toulouse, France
[b] Laboratoire d'étude du Comportement à Long Terme LCLT/SECM/DTCD CEA Valrhô BP17171, 30207 Bagnols-sur-Cèze cedex, France

Received 10 May 2005; accepted 13 January 2006

Abstract

The steady-state dissolution rates of Nd-britholite $Ca_9Nd(PO_4)_5SiO_4F_2$ have been measured at 25 °C as a function of aqueous solution composition in open-system mixed flow reactors. Measured Nd-britholite dissolution rates based on Ca, P, and F release are found to be close to corresponding apatite dissolution rates; these 25 °C rates decrease from 10^{-8} to 10^{-12} mol/m^2/s with increasing pH from 3 to 12. Measured Nd release rates are far slower than those of these other elements; Nd concentrations in solution appear to limited by precipitation of a secondary phosphate phase, which limits aqueous Nd concentrations to $<10^{-12}$ mol/kg at near neutral conditions. Correspondingly, it appears likely that aqueous actinide release from analogous waste hosts will be similarly limited by the precipitation of sparingly soluble phases.

1. Introduction

The motivation for this study is the assessment of apatite structured ceramics to serve as host for the storage of long-lived actinides. The apatite structure is believed to be well suited for radioactive actinide storage for a variety of reasons. First, 2 billion year old tri and tetravalent actinide bearing apatites have been found in the Oklo, Gabon natural nuclear reactor [1]. Secondly, the apatite structure is known to be relatively resistant to self-irradiation [2–4]. Thirdly, apatite minerals exhibit retrograde solubility with respect to temperature [5,6]. Lastly, apatite, with the generic formula $M_{10}(XO_4)_6Y_2$ (where $M = Ca^{2+}$, Pb^{2+}, Ba^{2+}, etc., $XO_4 = PO_4^{3-}, VO_4^{3-}, AsO_4^{3-}, SiO_4^{4-}$, etc., and $Y = F^-$, Cl^-, OH^-, Br^-, I^-, etc.), can readily incorporate tri and tetravalent actinides (Ac) in its structure through a double substitution of Ac(III,IV) for Ca(II) and SiO_4 for PO_4 leading to $Ca_{10-x}Ac(III)_x(PO_4)_{6-x}(SiO_4)_xF_2$ and $Ca_{10-x}Ac(IV)_x(PO_4)_{6-2x}(SiO_4)_{2x}F_2$ [7]. Many analogous rare-earth element minerals e.g., La [8], Ce and Eu [9], Nd [10,11], Pr and Sm [12] or actinides e.g., U [13,14], Th [14] have been synthesized.

Neodymium is frequently used as a chemical analogue for the actinide elements owing to its similar charge, size and chemistry [15–17]. As such a number of studies explored the properties of the

* Corresponding author. Tel.: +33 5 61 33 25 75; fax: +33 5 61 33 25 60.
E-mail address: oelkers@lmtg.obs-mip.fr (E.H. Oelkers).

0022-3115/$ - see front matter © 2006 Elsevier B.V. All rights reserved.
doi:10.1016/j.jnucmat.2006.01.022

$Ca_{10}(PO_4)_6Y_2$–$Ca_4Nd_6(SiO_4)_6Y_2$ solid solution [10,18–21]. This study focuses on the stability and reactivity of one component of this solid-solution series, Nd-britholite ($Ca_9Nd(PO_4)_5(SiO_4)F_2$). This phase has been described in detail by Guy et al. [7]. This composition has been chosen for this study because a 10% substitution of calcium for actinides has been suggested to be optimal for long-term waste storage [8]. To assess the ability of apatite structured actinide phases to resist to aqueous corrosion, both the steady-state dissolution rates and dissolution stoichiometry of Nd-britholite have been measured in open-system mixed flow reactors as a function of solution composition. Corresponding closed-system experiments have been preformed to estimate the solubility of this phase. The purpose of this communication is to present the results of this experimental study and to use the obtained data to evaluate the potential of apatite structured materials as long-term waste storage hosts.

2. Theoretical considerations

The standard state adopted in this study is that of unit activity for pure minerals and H_2O at any temperature and pressure. For aqueous species other than H_2O, the standard state is unit activity of the species in a hypothetical 1 molal solution referenced to infinite dilution at any temperature and pressure. To simplify the Nd-britholite stability calculation, it is assumed in the present study that it is the only constituent of the $Ca_{10}(PO_4)_6F_2$–$Ca_4Nd_6(SiO_4)_6F_2$ solid solution. The standard state for Nd-britholite, is therefore unit activity of $Ca_9Nd(PO_4)_5SiO_4F_2$. The dissolution of this phase can be described using

$$Ca_9Nd(PO_4)_5SiO_4F_2 + 4H^+ = 9Ca^{2+} + Nd^{3+} + 5PO_4^{3-} + SiO_2 + 2F^- + 2H_2O \quad (1)$$

Assuming the Nd-britholite composition remains invariant upon attainment of equilibrium (i.e. 'stoichiometric saturation' as defined by Thorstenson and Plummer [22] and Rabinowicz et al. [23]), the law of mass action for reaction (1) can be written

$$K = \frac{a^9_{Ca^{2+}} a_{Nd^{3+}} a^5_{PO_4^{3-}} a_{SiO_2} a^2_{F^-}}{a^4_{H^+}}, \quad (2)$$

where K designates an apparently equilibrium constant, and a_i represents the activity of the subscripted aqueous species.

The dissolution and crystallization rates of minerals can be described by considering transition state theory (TST). According to TST, the overall rate r of a mineral dissolution reaction per unit surface area can be described using [24,25]:

$$r = r_+\left(1 - \exp\left(-\frac{A}{\sigma RT}\right)\right), \quad (3)$$

where r_+ designates the forward dissolution rate per unit surface area, R denotes the gas constant, T stands for absolute temperature, A refers to the chemical affinity of the dissolution reaction, and σ represents Tempkin's average stoichiometric number equal to the ratio of the rate of destruction of the activated complex relative to the overall dissolution rate. The parenthetical term in Eq. (3) takes account the effect of the back reaction as equilibrium is approached and insures that $r = 0$ at equilibrium. The chemical affinity of reaction (1) is defined as

$$A = -RT\ln\left(\frac{Q}{K}\right) = -2.303RT\Omega, \quad (4)$$

where Q refers to the reaction activity quotient, and Ω represents the saturation index ($\Omega \equiv \log(Q/K)$). The form of Eq. (3) is such that overall rates (r) equal forward rates (r_+) when $A \gg \sigma RT$, but decrease continuously to 0 at equilibrium with decreasing A when $A < 3\sigma RT$.The variation of r_+ with solution composition depends on the dissolution mechanism of the mineral. Because the dissolution mechanism of many multi-oxide minerals includes the removal of metals from their structure via proton exchange reactions, these minerals exhibit forward dissolution rates that depend on the aqueous concentration of these constituent metals [26,27]. This possibility will be tested for the case of Nd-britholite by measuring its dissolution rates at far from equilibrium conditions as a function of aqueous Ca, P, and F concentration.

3. Materials and methods

The Nd-britholite used in this study was synthesized according to the method of Boyer et al. [8]; Nd-britholite was first formed from solid oxides and CaF_2 at 1400 °C according to the reaction:

$$0.5Nd_2O_3 + CaF_2 + 3CaO + 2.5Ca_2P_2O_7 + SiO_2 \rightarrow Ca_9Nd(PO_4)_5(SiO_4)F_2 \quad (5)$$

then naturally sintered. The resulting solid was analyzed by X-ray diffraction. The resulting diffraction

pattern is illustrated in Fig. 1 and matches closely that of reference Nd-britholite (file JCPDS 87-0480). The chemical composition of this solid was determined using a Camebax microprobe SX50 using 20 unique scan spots (see Table 1). The chemical formula of the synthesized Nd-britholite is found to be consistent with $Ca_{8.95}Nd_{0.93}(PO_4)_{5.01}(SiO_4)_{1.07}F_{1.08}OH_{0.30}$. This synthetic britholite was ground to 63–125 μm and 125–250 μm with an agate mortar and pestle and further sieved and cleaned ultrasonically 10 times with alcohol. A scanning electron microscope (SEM) image of the cleaned powder is shown in Fig. 2(a). The powder is found to be essentially free of fine particles. The BET surface area of these powders, as determined by eight point krypton adsorption using a Micrometrics ASAP 2010, is $604 \pm 10\ cm^2/g$ and $341 \pm 6\ cm^2/g$ for the 63–125 μm and 125–250 μm size fractions, respectively.

Both closed- and open-system experiments were performed in the present study. All experiments were performed in a 25 ± 1 °C temperature regulated room. Three closed-system experiments, aimed at determining the apparent solubility product of Nd-britholite were performed in 500 ml Nalgene® bottles. These closed-system experiments were initiated by placing Nd-britholite powder and initial solution into the reactors; the ratio of powder to solution in each experiment was chosen such that surface/solution ratio was equal to $S/V = 2.1\ cm^{-1}$. The reactors were sealed and placed on mechanical shaking table. Solutions were regularly collected using a syringe; these samples were filtered through a 0.45 μm Millipore® Nitrocellulose filter prior to analysis.

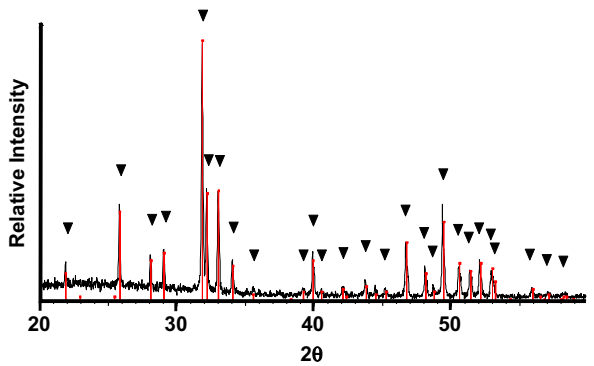

Fig. 1. XRD diffraction pattern of synthetic Nd-britholite. The radiation source was the CuK-α emission ray. Positions of the diffraction peaks of the reference Nd-britholite file JCPDS 87-0780 are shown by the symbol ▼.

Dissolution rates were measured in open-system, mixed-flow reactors consisting of 120 ml Savillex® fusion vessels [28]. These reactors were fitted with Nalgene® tubes for inlet and outlet fluid passage. Dissolution experiments were initiated by placing from 0.1 to 6 g of Nd-britholite powder into the reactors. The reactors were then filled with inlet solution, sealed, and the reactor attached to the inlet and outlet solution lines. The inlet solution was pumped into the reactors at a constant rate with Gilson® peristaltic pumps; all outlet fluids passed through a 0.45 μm Millipore® Nitrocellulose filter while exiting the reactors. Mounted teflon coated stirring bars were used to mix the powder/fluid mixture in the reactor from 150 to 250 rpm while avoiding powder grinding. Outlet solutions were collected regularly for analysis.

Inlet solutions were comprised of demineralized H_2O and sufficient Merck reagent grade NaCl, HCl, NaOH and/or NH_4OH to obtain the desired pH and an ionic strength of 0.01 M. Solutions containing calcium, phosphorus, or fluoride were prepared by the addition of $Ca(NO_3)_2$, KH_2PO_4, or NaF. Sample pH was measured at 25 °C within a few hours of sampling using a Metrohm® 744 pH-meter coupled to a Metrohm® Pt1000/B/2 electrode with a 3 M KCl outer filling solution. The electrode was calibrated with NBS standards at pH 4.01, 6.86, 9.22, and 11.00, with an average error <0.05 pH units. Calcium concentrations were measured by flame atomic absorption spectroscopy using a Perkin Elmer® 5100 with a detection limit 0.3 ppm and a precision of better than 3%. Fluoride

Table 1
Composition of the synthetic britholite used in the present study

	F	SiO_2	P_2O_5	Cl	CaO	Nd_2O_3	H_2O(c)	Sum Ox%
%	1.87	5.82	32.30	0.07	45.58	14.17	0.73	100.56
Uncertainty	0.27	0.59	0.97	0.03	0.71	1.17	0.12	0.72

Values are listed in oxide percent and were determined by microprobe analysis; reported values are the average of 10 scans. Sum Ox% refers to the sum of the measured compositions.

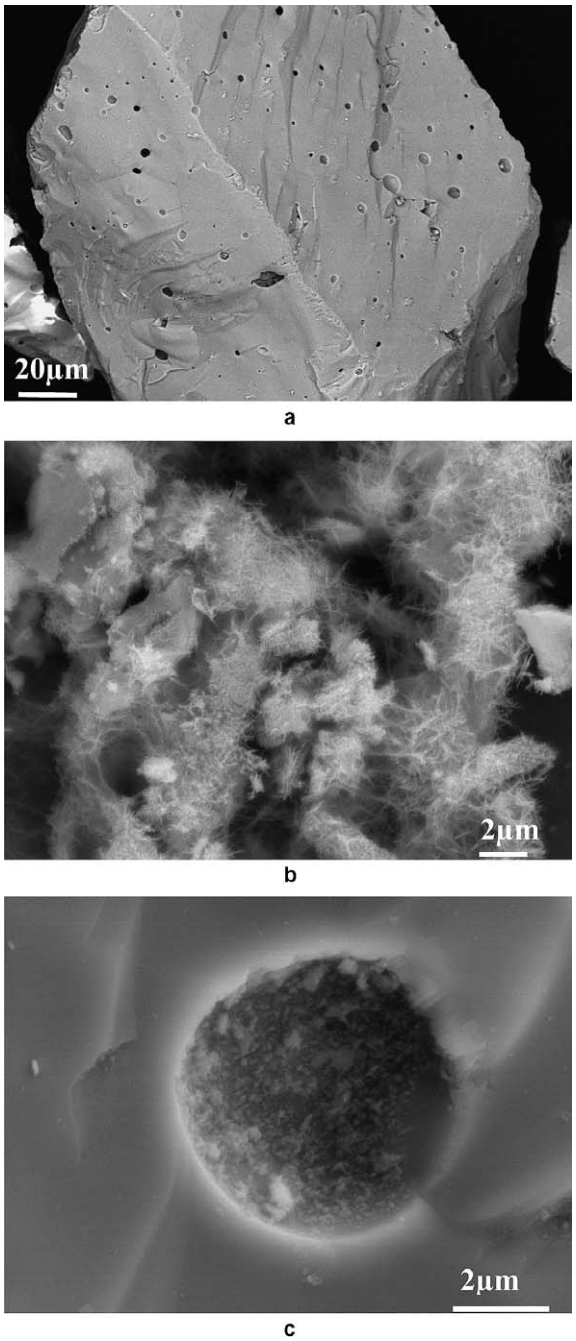

Fig. 2. SEM photographs of (a) Nd-britholite before experiment, (b) after dissolution in a closed system reactor during experiment B4BRI3, and (c) after dissolution in an open system reactor at basic pH during experiment BRI-14.

and phosphate analyses were determined with a Dionex high pressure liquid chromatography (HPLC) after elimination of chloride ions using DIONEX® Onguard II $AgNO_3$ cartridges with a detection limit of 0.1 and 0.3 ppm, respectively, and a precision of better than 8%. Concentrations of neodymium were determined with an Thermo Optek© PQ EXCELL inductive coupled plasma mass spectrometer with a detection limit 0.1 µg/kg and a precision of better than 5%. Silicon concentrations were determined with an inductive coupled plasma atomic emission spectrometer VISTA PRO VARIAN; the detection limit is 100 µg/l and an precision better than 6%.

Steady-state Nd-britholite dissolution rates were computed from measured steady-state outlet solution concentrations using

$$r_i = \frac{c_i F}{v_i S}, \tag{6}$$

where r_i refers to the Nd-britholite dissolution rate based on the release rate of the ith element, c_i stands for the outlet concentration of the ith element, F represents the fluid flow rate, v_i denotes a stoichiometric coefficient equal to the number of moles of the ith element present in one mole of Nd-britholite, and S denotes the total Nd-britholite surface area present in the reactor. S was calculated by multiplying the mass of powder in the reactor by the powder's initial specific BET surface area.

4. Results

4.1. Closed-system experiments

In an attempt to estimate the 25 °C solubility constant of neodymium britholite three closed-system experiments were run. The results of these experiments are listed in Table 2. The temporal solution composition evolution during the closed-system experiments are shown in Fig. 3. All measured reactive solution concentrations attain a stationary state after ~50 days of elapsed time. The Nd-britholite reaction quotient (Q) and the saturation index (Ω) for possible secondary phases in all reactive solutions were computed using PHREEQC together with the LLNL [29] database. Solubility products of potential secondary products likely to precipitate are listed in Table 3; the saturation index of experimental solutions with respect to these phases are presented in Table 4. No phase is supersaturated other than hydroxylapatite. Although a precipitate was observed on the surface of the britholite after these closed-system experiments, its composition and habit was inconsistent with hydroxylapatite precipitation (see below).

Table 2
Results of all closed-system Nd-britholite dissolution experiments performed in the present study

Sample number	Elapsed time (days)	pH	Measured concentrations					Log(Q)
			Ca (μmol/kg) ±3%	P (μmol/kg) ±8%	F (μmol/kg) ±8%	Si (μmol/kg) ±6%	Nd (μmol/kg) ±5%	
B4BRI3-1	0.0	3.1	30.38	ND	ND	ND	ND	−146
B4BRI3-2	3.0	3.7	423.80	202.45	ND	47.09	1.6708	−117
B4BRI3-3	6.9	4.2	523.19	249.25	ND	60.49	0.0915	−109
B4BRI3-4	10.2	4.5	542.59	ND	ND	63.73	0.0130	−105
B4BRI3-5	16.9	5.0	555.90	252.73	ND	66.12	0.0016	−99
B4BRI3-6	23.9	5.4	541.46	277.72	ND	67.33	$<7\times10^{-4}$	−97
B4BRI3-7	30.9	5.7	564.77	274.89	ND	67.97	$<7\times10^{-4}$	−94
B4BRI3-8	34.9	5.7	551.03	271.71	ND	66.90	$<7\times10^{-4}$	−94
B4BRI3-9	42.1	5.9	530.67	272.43	ND	69.04	$<7\times10^{-4}$	−92
B4BRI3-10	61.9	5.9	543.99	278.44	ND	73.49	$<7\times10^{-4}$	−92
B4BRI3-11	70.0	5.8	590.47	279.60	ND	75.70	$<7\times10^{-4}$	−92
B4BRI3-12	80.9	5.9	573.98	277.21	ND	75.70	$<7\times10^{-4}$	−92
B4BRI3-13	93.9	5.9	572.78	270.85	ND	73.95	$<7\times10^{-4}$	−91
B5BRI4-1	0.0	4.1	6.16	3.42	ND	ND	0.0622	−143
B5BRI4-2	3.0	6.9	115.93	64.41	ND	16.34	$<7\times10^{-4}$	−91
B5BRI4-3	6.9	7.2	150.14	71.88	ND	20.08	$<7\times10^{-4}$	−87
B5BRI4-4	10.2	7.1	161.99	79.85	ND	23.14	$<7\times10^{-4}$	−87
B5BRI4-5	16.9	7.4	189.87	97.53	ND	58.07	$<7\times10^{-4}$	−83
B5BRI4-6	23.9	7.5	220.66	107.03	ND	33.18	$<7\times10^{-4}$	−81
B5BRI4-7	30.9	7.5	266.95	129.19	ND	37.88	$<7\times10^{-4}$	−80
B5BRI4-8	34.9	7.5	281.42	141.76	ND	40.38	$<7\times10^{-4}$	−80
B5BRI4-9	42.1	7.7	307.21	150.87	ND	42.33	$<7\times10^{-4}$	−77
B5BRI4-10	61.9	7.4	337.77	164.89	ND	48.60	$<7\times10^{-4}$	−79
B5BRI4-11	70.0	7.2	335.64	162.36	ND	49.28	$<7\times10^{-4}$	−81
B5BRI4-12	80.9	7.4	339.31	168.97	ND	51.84	$<7\times10^{-4}$	−80
B5BRI4-13	93.9	7.4	331.94	166.58	ND	52.48	$<7\times10^{-4}$	−79
B6BRI5-1	0.0	5.1	2.55	ND	ND	ND	$<7\times10^{-4}$	−139
B6BRI5-2	3.0	8.2	84.89	ND	ND	ND	$<7\times10^{-4}$	−81
B6BRI5-3	6.9	7.7	106.90	ND	ND	15.99	$<7\times10^{-4}$	−84
B6BRI5-4	10.2	7.5	126.85	ND	ND	20.47	$<7\times10^{-4}$	−84
B6BRI5-5	16.9	7.8	169.52	81.64	ND	25.49	$<7\times10^{-4}$	−81
B6BRI5-6	23.9	7.7	205.30	103.51	ND	29.94	$<7\times10^{-4}$	−80
B6BRI5-7	30.9	7.6	250.99	130.28	ND	34.96	$<7\times10^{-4}$	−79
B6BRI5-8	34.9	7.6	276.77	140.82	ND	37.60	$<7\times10^{-4}$	−79
B6BRI5-9	42.1	7.8	298.46	158.40	ND	47.07	$<7\times10^{-4}$	−76
B6BRI5-10	61.9	7.6	353.82	178.43	ND	50.24	$<7\times10^{-4}$	−77
B6BRI5-11	70.0	7.4	351.41	173.39	ND	51.70	$<7\times10^{-4}$	−79
B6BRI5-12	80.9	7.5	348.11	178.52	ND	52.55	$<7\times10^{-4}$	−78
B6BRI5-13	93.9	7.5	338.08	180.70	ND	ND	ND	−78

ND: Non-determined.

The reactive fluid pH increases as Nd-britholite dissolves due to proton consumption consistent with reaction (1). The relative concentrations of Ca and Si in the reactive fluid are consistent with their stoichiometric release from the original Nd-britholite. In contrast, as can be seen in Fig. 3, the P/Ca, ratios of the reactive fluid are distinctly lower than that of the dissolving initial solid, suggesting P incorporation in a secondary solid. The Nd/Ca ratios are also far lower than that of the dissolving Nd-britholite. These ratios are always at least four times lower than that of dissolving solid. Insight into the identity of the precipitating secondary phase can be obtained from analysis of the solids after these closed-system experiments. A representative photomicrograph of the solids recovered after these closed-system experiments is shown in Fig. 2(b). The initial britholite is found to be covered with a fibrous precipitate. EDS analysis of this precipitate shows it to be rich in Nd and P.

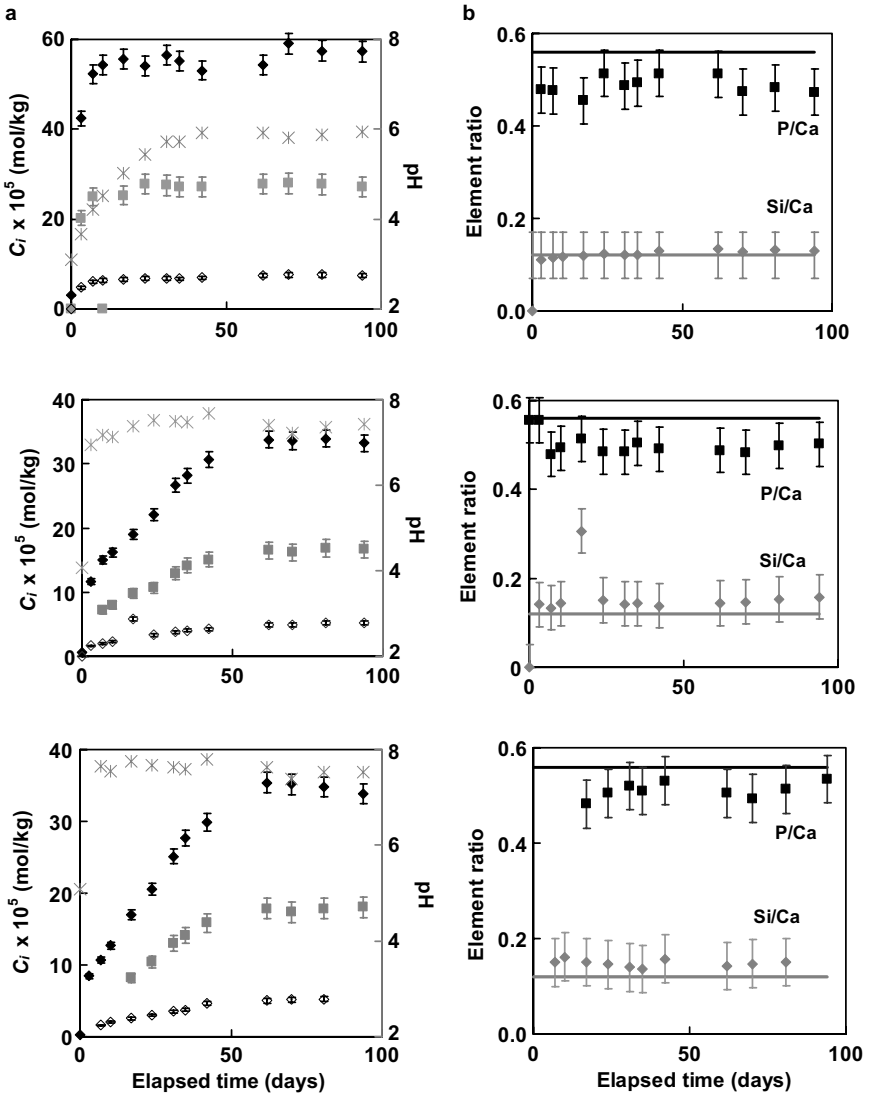

Fig. 3. Fluid composition evolution during experiments B4BRI3, B5BRI4, and B6BRI5: (a) temporal evolution of calcium (◆); phosphorus (■) and silicon (◊) concentration, and pH (∗). The error bars surrounding the data points on this figure correspond to the analytic uncertainty on measured concentrations (±3% for Ca, ±8% for P, and ±6% for Si). (b) Temporal evolution of atomic P/Ca (■) and Si/Ca (◆) ratio. The solid lines in (b) represent the corresponding concentrations in the solid phase. The error bars on this figure correspond to a ±0.05 uncertainty on these ratios.

4.2. Open-system experiments

Thirty-eight open-system experiments were performed in the present study to quantify the variation Nd-britholite dissolution rates as a function of solution composition. The results of these experiments are presented in Table 5. Nd-britholite dissolution rates based on the release of all elements were computed using Eq. (6). As shown in Table 6, outlet fluids were undersaturated with respect to all potential secondary phases other than apatite, $NdPO_4$(c), and $Nd(OH)_3$(c). The degree of outlet fluid saturation with respect to $NdPO_4$(c) and $Nd(OH)_3$(c) are difficult to assess because the aqueous Nd concentration is commonly below the analytic detection limit. Nd concentrations were only determined in the outlet solutions of experiments BRI-01 and BRI-02. $NdPO_4$(c) is found to be strongly supersaturated in these solutions. This observation and the observation that Nd is preferentially incorporated

Table 3
Solubility product of different phases tested as potential secondary products during experiment [29]

Name	Formula	Equation	Log K
Fluorapatite	$Ca_5(PO_4)_3F$	$Ca_5(PO_4)_3F + 3H^+ = 5Ca^{2+} + 3HPO_4^{3-} + F^-$	−25.0
Hydroxyapatite	$Ca_5(PO_4)_3OH$	$Ca_5(PO_4)_3OH + 4H^+ = 5Ca^{2+} + 3HPO_4^{3-} + H_2O$	−3.1
Quartz	SiO_2	$SiO_2 = SiO_2$	−4.0
Whitlockite	$Ca_3(PO_4)_2$	$Ca_3(PO_4)_2 + 2H^+ = +2HPO_4^{2-} + 3Ca^{2+}$	−4.2
Brushite	$CaHPO_4 \cdot 2H_2O$	$CaHPO_4 : 2H_2O = Ca^{2+} + HPO_4^{2-} + 2H_2O$	6.6
Wollastonite	$CaSiO_3$	$CaSiO_3 + 2H^+ = Ca^{2+} + H_2O + SiO_2$	13.8
Pseudo-wollastonite	$CaSiO_3$	$CaSiO_3 + 2\ H^+ = Ca^{2+} + H_2O + SiO_2$	14.0
Portlandite	$Ca(OH)_2$	$Ca(OH)_2 + 2H^+ = Ca^{2+} + 2H_2O$	22.6
Okenite	$CaSi_2O_4(OH)_2 \cdot H_2O$	$CaSi_2O_4(OH)_2{:}H_2O + 2H^+ = Ca^{2+} + 2SiO_2 + 3H_2O$	10.4
Hatrurite	Ca_3SiO_5	$Ca_3SiO_5 + 6H^+ = SiO_2 + 3Ca^{2+} + 3H_2O$	73.4
Larnite	Ca_2SiO_4	$Ca_2SiO_4 + 4H^+ = SiO_2 + 2Ca^{2+} + 2H_2O$	38.5
Afwillite	$Ca_3SiO_2O_4(OH)_6$	$Ca_3Si_2O_4(OH)_6 + 6H^+ = 2SiO_2 + 3Ca^{2+} + 6H_2O$	60.0

in solid phases during these experiments suggest that all outlet solutions were supersaturated with respect to either $NdPO_4$(c) and/or $Nd(OH)_3$(c).

An example of the temporal evolution of measured Nd-britholite dissolution rates during a typical open-system experiment are shown in Fig. 4. During the initial transient time period, calcium and fluoride are preferentially released whereas phosphorus and silicon are preferentially retained by the solid. After ~1 day, outlet fluid concentration attains a steady state. Steady-state dissolution rates based on the outlet fluid composition of calcium and fluoride are identical within analytical uncertainty. Rates based on silicon concentration are at the most part within 50% those deduced based on Ca and F concentration. Rates based on outlet fluid phosphorus concentrations are slightly lower than those based on Si, Ca, and F. Most impressively, steady-state Nd-britholite dissolution rates based in outlet fluid Nd concentrations are at least an order of magnitude slower than those based on Ca, Si, F, or P which suggests its probable incorporation in secondary products. These relative release rates are thus globally consistent with those of the closed-system experiments, which also exhibit the preferential incorporation of Nd and, to a lesser extent, P in solid phases.

Further insight into the process responsible for the retention of Nd in the solid phase during the open-system experiments can be obtained by considering the relative release rates of P. Steady-state Nd-britholite dissolution rates based on P release for all experiments performed in P-free inlet solutions are depicted as a function of their corresponding rates based on Ca release in Fig. 5. It can be seen in this figure that dissolution rates based on P release are typically 8–15% less than those based on Ca release. This observation suggests the co-precipitation of Nd with P during these open-system experiments.

The variation of 25 °C steady-state Nd-britholite dissolution rates based on outlet fluid Ca release obtained in Ca, P, and F-free inlet solutions are presented in Fig. 6. Rates decrease monotonically with increasing pH from pH 3 to 7. A linear least squares fit of the data from pH 3 to 12 yields

$$r_{Ca}/(\mathrm{mol/m^2\ s}) = 10^{-6.5} a_{H^+}^{0.5} + 10^{-10.4}. \quad (7)$$

Note the rates at pH > 8 are assumed to be constant in this equation although a further decrease in the rates is suggested by the data at pH > 10. The rate data obtained in the present study are, however, insufficiently constrained to warrant a more detailed interpretation due to the uncertainties of the chemical affinity on these rates.

Further experiments were performed at pH 3 to assess the degree to which Nd-britholite dissolution rates are influenced by reactive fluid calcium, phosphorus, and fluoride concentrations. The results of these experiments are illustrated in Fig. 7. These results demonstrate, that in contrast with many other multi-oxide minerals, the dissolution rates of Nd-britholite are independent of reactive fluid calcium, phosphorus, and fluoride concentration at far from equilibrium conditions.

The surfaces of the solids recovered after the open-system experiments were analyzed by scanning electron microscopy. Similar to the solids recovered in the closed-system experiments, those recovered from the open-system experiments were found to be covered with a fibrous Nd–P-rich secondary phase. Samples recovered from experiments performed at pH > 11 also contained amorphous precipitates

Table 4
Saturation index (Log(Q/K)) of potential secondary products during closed-system experiments

Ref	Saturation index (Ω)										
	Hydroxylapatite	Quartz	Whitlockite	Brushite	Wollastonite	Pseudo-wollastonite	Portlandite	Okenite	Hatrurite	Larnite	Afwillite
B4BRI3-1							−21.3				
B4BRI3-2	−22.8	−0.3	−14.3	−17.7	−14.4	−14.7	−18.9	−15.3	−66.8	−35.5	−57.7
B4BRI3-3	−18.6	−0.2	−11.8	−17.0	−13.2	−13.5	−17.8	−14.0	−63.4	−33.2	−54.2
B4BRI3-4		−0.2			−12.6	−12.8	−17.2	−13.4	−61.5	−31.9	−52.3
B4BRI3-5	−12.9	−0.1	−8.5	−16.1	−11.6	−11.8	−16.2	−12.3	−58.5	−29.9	−49.3
B4BRI3-6	−10.0	−0.1	−6.9	−15.7	−10.8	−11.0	−15.4	−11.5	−56.1	−28.3	−46.9
B4BRI3-7	−7.9	−0.1	−5.7	−15.4	−10.1	−10.4	−14.8	−10.9	−54.3	−27.1	−45.0
B4BRI3-8	−8.0	−0.1	−5.7	−15.4	−10.2	−10.4	−14.8	−10.9	−54.3	−27.1	−45.1
B4BRI3-9	−6.7	−0.1	−5.0	−15.3	−9.8	−10.0	−14.4	−10.5	−53.1	−26.3	−43.9
B4BRI3-10	−6.6	−0.1	−5.0	−15.3	−9.7	−10.0	−14.4	−10.4	−53.1	−26.3	−43.8
B4BRI3-11	−7.1	−0.1	−5.2	−15.3	−9.9	−10.1	−14.6	−10.6	−53.6	−26.6	−44.3
B4BRI3-12	−6.5	−0.1	−4.9	−15.2	−9.7	−9.9	−14.4	−10.4	−53.0	−26.2	−43.7
B4BRI3-13	−6.6	−0.1	−4.9	−15.3	−9.7	−9.9	−14.4	−10.4	−53.0	−26.2	−43.7
B5BRI4-1	−34.5		−21.7	−20.9							
B5BRI4-2	−5.8	−0.8	−4.9	−15.9	−9.0	−9.3	−13.1	−10.4	−49.7	−24.3	−41.1
B5BRI4-3	−3.6	−0.7	−3.6	−15.6	−8.2	−8.5	−12.4	−9.5	−47.5	−22.8	−38.8
B5BRI4-4	−3.8	−0.6	−3.7	−15.6	−8.3	−8.6	−12.5	−9.6	−48.0	−23.0	−39.2
B5BRI4-5	−1.8	−0.2	−2.6	−15.3	−7.3	−7.5	−11.9	−8.1	−45.6	−21.3	−36.4
B5BRI4-6	−0.9	−0.5	−2.1	−15.2	−7.3	−7.5	−11.6	−8.3	−45.0	−21.0	−36.1
B5BRI4-7	−0.2	−0.4	−1.7	−15.1	−7.1	−7.4	−11.5	−8.1	−44.7	−20.8	−35.7
B5BRI4-8	**0.0**	−0.4	−1.5	−15.0	−7.1	−7.3	−11.5	−8.1	−44.6	−20.7	−35.6
B5BRI4-9	**1.1**	−0.4	−0.9	−14.9	−6.6	−6.9	−11.1	−7.6	−43.3	−19.8	−34.3
B5BRI4-10	**0.1**	−0.3	−1.4	−14.9	−7.1	−7.4	−11.6	−8.0	−44.9	−20.9	−35.8
B5BRI4-11	−0.8	−0.3	−1.9	−14.9	−7.5	−7.7	−12.0	−8.4	−46.1	−21.7	−37.0
B5BRI4-12	**0.2**	−0.3	−1.4	−14.9	−7.1	−7.3	−11.6	−8.0	−44.9	−20.9	−35.8
B5BRI4-13	**0.1**	−0.3	−1.4	−14.9	−7.1	−7.3	−11.6	−8.0	−44.9	−20.9	−35.8
B6BRI5-1							−18.3				
B6BRI5-2							−10.6				
B6BRI5-3		−0.8			−7.5	−7.7	−11.5	−8.9	−45.1	−21.2	−36.5
B6BRI5-4		−0.7			−7.7	−7.9	−11.8	−9.0	−45.9	−21.7	−37.2
B6BRI5-5	−0.5	−0.6	−2.0	−15.4	−6.9	−7.1	−11.1	−8.1	−43.7	−20.2	−34.9
B6BRI5-6	−0.2	−0.5	−1.7	−15.2	−6.9	−7.2	−11.2	−8.1	−43.9	−20.3	−35.1
B6BRI5-7	**0.1**	−0.4	−1.5	−15.1	−7.0	−7.2	−11.3	−8.0	−44.2	−20.5	−35.3
B6BRI5-8		−0.4	−1.3	−15.0	−6.9	−7.2	−11.3	−7.9	−44.1	−20.4	−35.1
B6BRI5-9	**1.6**	−0.3	−0.7	−14.9	−6.4	−6.6	−10.9	−7.3	−42.7	−19.4	−33.6
B6BRI5-10	**1.2**	−0.3	−0.8	−14.8	−6.7	−6.9	−11.2	−7.6	−43.6	−20.0	−34.5
B6BRI5-11	**0.3**	−0.3	−1.3	−14.8	−7.1	−7.3	−11.6	−8.0	−44.8	−20.8	−35.7
B6BRI5-12	**0.7**	−0.3	−1.0	−14.8	−6.9	−7.1	−11.4	−7.7	−44.2	−20.4	−35.1
B6BRI5-13	**0.7**		−1.1	−14.8			−11.4				

Table 5
Results of all open-system Nd-britholite dissolution experiments performed in the present study

Experiment number	Solution	Inlet solution (μmol/kg)			pH inlet	pH outlet	S (cm^2)	Flow rate (mg/s)	Outlet solution (μmol/kg)					r_{Ca} (×10^{10} mol/m^2 s)	r_P (×10^{10} mol/m^2 s)	r_F (×10^{10} mol/m^2 s)	r_{Nd} (×10^{10} mol/m^2 s)	r_{Si} (×10^{10} mol/m^2 s)	A[a] (kJ/mol)
		C_{Ca} ±3%	C_P ±8%	C_F ±8%					C_{Ca} ±3%	C_P ±8%	C_F ±8%	C_{Nd} ±5%	C_{Si} ±6%						
BRI-01	HCl/NaCl	0	0	0	3.0	3.3	151	4.7	332	153	36.3	2.59	52.8	114	93.6	103	7.87	149	256
BRI-02	HCl/NaCl	0	0	0	3.0	3.3	150	5.3	281	136	35.2	2.42	40.5	110	95.7	115	0.02	132	262
BRI-03	HCl/NaCl	0	0	0	2.9	3.9	688	4.2	665	–	–	–	–	45.0	–	–	–	–	502
BRI-04	HCl/NaCl	0	0	0	3.1	4.3	1353	2.0	611	332	–	–	–	10.2	10.0	–	–	–	177
BRI-05	HCl/NaCl	0	0	0	3.1	4.3	1353	2.8	615	325	6.84	–	–	14.0	13.2	1.33	–	–	189
BRI-06	HCl/NaCl	0	0	0	3.4	4.4	651	4.2	192	–	–	–	–	13.7	–	–	–	–	216
BRI-07	HCl/NaCl	0	0	0	–	5.5	647	4.2	43.8	34.6	5.53	–	–	3.10	4.39	3.26	–	–	195
BRI-08	MQ/NaCl	0	0	0	4.1	6.3	735	2.3	78.0	24.7	3.53	<DL	14.6	2.78	1.55	1.05	–	0.52	132
BRI-09	MQ/NaCl	0	0	0	4.7	6.6	419	2.5	32.2	14.0	3.11	–	–	2.12	1.64	1.69	–	–	142
BRI-10	MQ/NaCl	0	0	0	5.0	6.9	1653	4.0	46.6	50.9	2.84	–	–	1.25	0.99	0.63	–	–	111
BRI-11	NH_4OH/NH_4Cl	0	0	0	–	9.8	1215	2.6	27.5	<DL	<DL	–	–	0.64	–	–	–	–	−11
BRI-12	NH_4OH/NH_4Cl	0	0	0	9.9	9.8	2332	2.6	42.4	<DL	<DL	<DL	38.4	0.53	–	–	–	3.98	−32
BRI-13	NaOH/NaCl	0	0	0	10.4	10.2	1215	2.6	22.4	<DL	<DL	–	–	0.52	–	–	–	–	−18
BRI-14	NaOH/NaCl	0	0	0	12.8	11.7	3529	1.8	5.75	3.55	<DL	–	–	0.03	0.04	–	–	–	−10
BRI-15	NaOH/NaCl	0	0	0	11.8	11.8	3529	3.5	7.85	2.90	2.84	–	–	0.09	0.06	0.27	–	–	−25
BRI-16	HCl/NaCl	33.5	0	0	2.9	3.3	153	5.2	352	152	32.4	–	–	121	103	102	–	–	275
BRI-17	HCl/NaCl	194	0	0	3.0	3.3	138	5.1	489	138	37.9	–	–	121	101	129	–	–	268
BRI-18	HCl/NaCl	294	0	0	3.0	3.2	122	5.0	545	123	34.7	–	–	113	99	130	–	–	275
BRI-19	HCl/NaCl	406	0	0	2.9	3.2	105	4.8	645	150	34.2	–	–	125	112	149	–	–	272
BRI-50	HCl/NaCl	504	0	0	2.9	3.3	152	5.4	802	128	28.3	–	–	118	91.2	93.0	–	–	260
BRI-21	HCl/NaCl	642	0	0	3.0	3.2	137	5.3	862	97.9	26.2	–	–	94.4	75.2	93.1	–	–	269
BRI-22	HCl/NaCl	695	0	0	3.0	3.2	125	5.2	912	104	26.8	–	–	99.9	86.2	104	–	–	267
BRI-23	HCl/NaCl	792	0	0	2.9	3.2	110	5.2	947	108	25.8	–	–	81.2	102	112	–	–	266
BRI-24	HCl/NaCl	0	49.2	0	2.9	3.4	153	5.4	362	182	39.5	–	–	143	94.2	129	–	–	263
BRI-25	HCl/NaCl	0	98.7	0	3.0	3.3	134	5.3	346	227	39.7	–	–	151	100	144	–	–	270
BRI-26	HCl/NaCl	0	158	0	3.0	3.3	115	5.2	296	256	39.5	–	–	149	89	164	–	–	273
BRI-27	HCl/NaCl	0	221	0	3.0	3.2	94	5.2	256	291	36.3	–	–	158	77	186	–	–	283
BRI-28	HCl/NaCl	0	226	0	2.9	3.4	152	5.4	369	400	45.1	–	–	147	124	149	–	–	254
BRI-29	HCl/NaCl	0	278	0	3.0	3.3	134	5.3	341	418	38.4	–	–	153	110	140	–	–	264
BRI-30	HCl/NaCl	0	333	0	3.0	3.3	115	5.2	290	476	40.5	–	–	146	129	169	–	–	267
BRI-31	HCl/NaCl	0	349	0	3.0	3.2	94	5.2	248	473	35.8	–	–	152	136	181	–	–	279
BRI-32	HCl/NaCl	0	444	0	2.9	3.4	152	5.4	398	635	49.9	–	–	158	136	165	–	–	248
BRI-33	HCl/NaCl	0	518	0	3.0	3.4	133	5.3	369	716	52.0	–	–	164	153	192	–	–	248
BRI-34	HCl/NaCl	0	506	0	3.1	3.3	113	5.2	270	650	40.0	–	–	139	132	171	–	–	265
BRI-35	HCl/NaCl	0	0	41.1	2.9	3.2	153	5.3	243	111	73.6	–	–	94.1	77.0	104	–	–	290
BRI-36	HCl/NaCl	0	0	92.6	3.0	3.2	141	5.1	502	92.7	122	–	–	80.5	66.2	96.6	–	–	294
BRI-37	HCl/NaCl	0	0	169	3.1	3.2	131	5.0	164	76.8	193	–	–	70.3	58.9	83.0	–	–	298
BRI-38	HCl/NaCl	0	0	218	3.0	3.2	119	5.0	144	64.2	242	–	–	67.1	53.9	90.1	–	–	302

<DL: below to detection limit; MQ: Milli-Q water.

[a] A is calculated from Eq. (4) assuming $\mathrm{Log}(K) = -79$.

Table 6
Saturation index (Log(Q/K)) of potential secondary products during opened system experiments

	Saturation index (Ω)												
	Fluorapatite	Hydroxy-apatite	Quartz	Whitlockite	Brushite	Fluorite	Wollastonite	Pseudo-wollastonite	Portlandite	Okenite	Hatrurite	Larnite	Afwillite
BRI-01	−12.7	−26.6	−0.2	−16.5	−18.3	−3.3	−15.3	−15.5	−19.8	−16.1	−69.5	−37.2	−60.3
BRI-02	−13.2	−27.1	−0.4	−16.8	−18.4	−3.4	−15.5	−15.7	−19.9	−16.4	−69.8	−37.5	−60.8
BRI-03													
BRI-04		−17.2		−11.0	−16.7								
BRI-05	−4.9	−17.2		−11.0	−16.7	−4.2							
BRI-06													
BRI-07	−6.4	−17.5		−11.6	−17.6	−5.4							
BRI-08	−1.3	−11.4	−0.8	−8.1	−16.8	−5.6	−10.5	−10.7	−14.5	−11.9	−53.9	−27.1	−45.3
BRI-09	−2.5	−12.3		−8.8	−17.3	−6.1			−14.2				
BRI-10	**0.1**	−9.3		−7.0	−16.8	−6.0			−13.5				
BRI-11									−7.9				
BRI-12			−1.0				−4.0	−4.2	−7.7	−5.6	−33.9	−13.8	−25.6
BRI-13									−7.2				
BRI-14		**2.4**		−2.1	−18.6				−4.9				
BRI-15	**7.4**	**3.0**		−1.9	−18.7	−6.8			−4.5				
BRI-16	−12.6	−26.5		−16.4	−18.3	−3.4			−19.8				
BRI-17	−12.0	−25.9		−16.0	−18.2	−3.1			−19.7				
BRI-18	−12.6	−26.5		−16.4	−18.3	−3.2			−19.8				
BRI-19	−12.3	−26.2		−16.2	−18.2	−3.2			−19.7				
BRI-50	−30.3		−18.0	−3.2			−19.4						
BRI-21	−32.0		−18.2	−3.3			−19.6						
BRI-22	−31.6		−18.1	−3.2			−19.6						
BRI-23	−31.4		−18.1	−3.2			−19.6						
BRI-24	−31.2		−18.1	−3.1			−19.6						
BRI-25	−32.1		−18.1	−3.2			−19.8						
BRI-26	−32.5		−18.1	−3.3			−19.9						
BRI-27	−34.2		−18.2	−3.5			−50.1						
BRI-28	−28.9		−17.7	−3.0			−19.6						
BRI-29	−30.6		−17.9	−3.3			−19.8						
BRI-30	−30.9		−17.9	−3.3			−19.9						
BRI-31	−33.0		−18.0	−3.5			−50.2						
BRI-32	−27.3		−17.5	−2.9			−19.5						
BRI-33	−27.3		−17.5	−2.9			−19.6						
BRI-34	−30.4		−17.8	−3.3			−19.9						
BRI-35	−36.3		−18.7	−2.9			−50.2						
BRI-36	−37.1		−18.8	−2.6			−50.2						
BRI-37	−38.1		−19.0	−2.3			−50.3						
BRI-38	−38.9		−19.2	−2.1			−50.4						

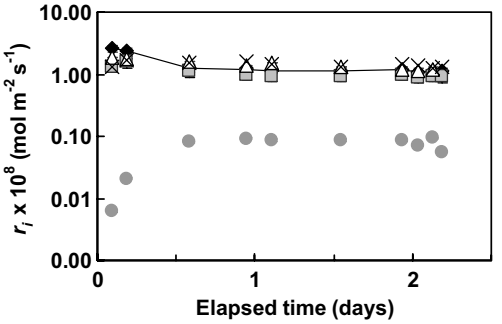

Fig. 4. Fluid composition evolution during open-system experiment BRI-01. The symbols ◆, ■, △, ×, and ● designate the concentrations of calcium, phosphorus, fluoride, silicon, and neodymium, respectively. The uncertainty of the measurements are approximated by the size of the symbols.

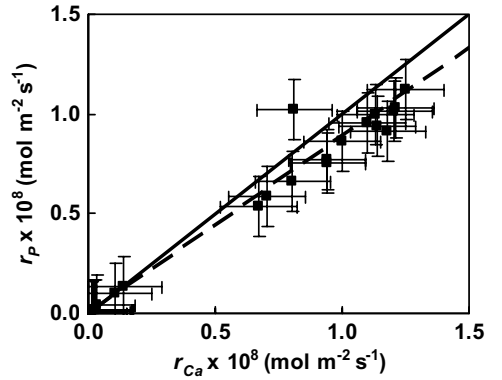

Fig. 5. Nd-britholite dissolution rates based on P release as a function of the corresponding rates based on Ca release. The solid line corresponds to stoichiometric dissolution of Nd-britholite in accord with reaction (1), whereas the dashed line corresponds to the stoichiometry of Nd-britholite dissolution coupled to Nd-rhabdophane precipitation in accord with reaction (8). The error bars surrounding the data points in this figure correspond to a $\pm 0.015 \times 10^8$ mol/m^2 s uncertainty in measured rates.

within the small pores present on the original Nd-britholite surfaces. A photomicrograph of these amorphous precipitates is shown in Fig. 2(c).

5. Discussion

5.1. Secondary phase identification

Secondary minerals often control the mobility of heavy metals [30]. Consequently, particular attention has been made to identify the secondary phases formed during the Nd-britholite dissolution experiments. The low Nd release rate and the relatively

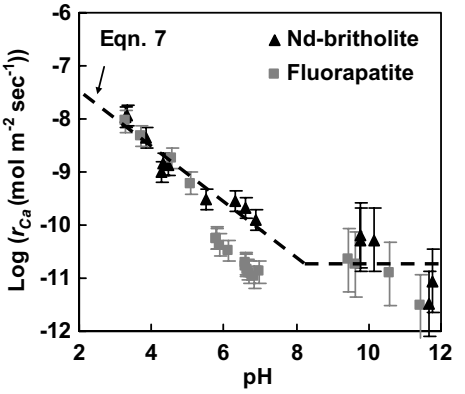

Fig. 6. Steady-state dissolution rates versus pH at 25 °C of Nd-britholite measured in the present study and of natural fluorapatite [44]. The error bars surrounding the data points in this figure correspond to a ±30% uncertainty in measured dissolution rates in acidic media and ±50% in basic media.

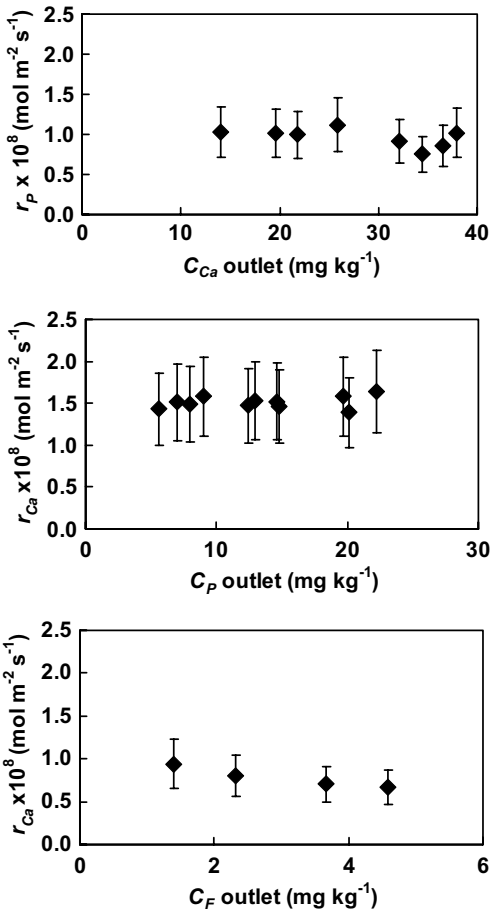

Fig. 7. Steady-state Nd-britholite dissolution rates as a function of the reactive solution concentration of calcium, phosphorus, and fluoride at 25 °C and pH = 3. The error bars surrounding the data points in this figure correspond to a ±30% uncertainty in measured dissolution rates.

low phosphorus release suggest Nd retention by the precipitation of a neodymium phosphate phase. Secondary rare-earth element phosphates were also observed to precipitate during the dissolution of apatite [28,31], monazite and xenotime [32], granites [33–35], rare-earth element/thorium phosphate diphosphate solid solutions [36], and nuclear waste glass [37]. The rare-earth phosphate phase precipitated in these studies is commonly identified as rhabdophane ($REE(PO_4)\cdot nH_2O$) due to its estimated solubility product. More recently, it has been shown that the solubility product of monazite, ($REEPO_4$) is similar to that of rhabdophane [38] suggesting that it too could precipitate during these experiments.

Clavier [39] showed that the structure of precipitated rare earth element phosphates depends strongly on the ionic radius of the cation and temperature. At low temperatures, the precipitate is rhabdophane structured while at higher temperature, rhabdophane rapidly changes into monazite following this precipitation. The temperature delimiting these two behaviors depends on the ionic radius of the rare-earth element, and ranges from 100 °C for La, 120 °C for Ce to 150 °C for Pr. Taking account of this trend, it seems likely that the delimiting temperature for Nd-phosphates occurs at $T > 150$ °C [40]. This suggests that the Nd-phosphate secondary phase precipitated in the present study is rhabdophane. This suggestion is also supported by the form of the precipitate observed by SEM on the post-experiment solids, as shown in Fig. 2(b). This precipitate consists of needle-shaped crystals; this morphology is consistent with the rhabdophane structure rather than that of monazite which precipitates as hexagonal crystals [36].

Taking account of the likelihood that the bulk of the Nd released by Nd-britholite in these experiments precipitated as Nd-rhabdophane, one can write the overall reaction:

$$Ca_9Nd(PO_4)_5SiO_4F_2 + 4H^+ + nH_2O = 9Ca^{2+} + SiO_{2(aq)} + 2F^- + 4PO_4^{-3} + 2H_2O + NdPO_4\cdot nH_2O \quad (8)$$

This reaction suggests that the reactive fluid concentration has a P/Ca ratio of 4/9 rather than the 5/9 that would stem from stoichiometric Nd-britholite dissolution. It can be seen in Fig. 5 that although a 5/9 P/Ca ratio can describe the compositions of the outlet solutions within uncertainty, these compositions are more consistent with a 4/9 P/Ca ratio as prescribed by reaction (8).

This conclusion and the results presented above suggests that neodymium is readily incorporated into Nd-rhabdophane during the low temperature dissolution of Nd-britholite. This conclusion is consistent with the results of PHREEQC calculations performed with the LLNL [29] database after adding the solubility products of rhabdophane taken from [41] and of monazite taken from [36]. These calculations show that all outlet or reactive solutions for which Nd was measurable are supersaturated with respect to Nd-rhabdophane. In basic media, solutions are predicted to be supersaturated with respect to $Nd(OH)_3$. Although this precipitate has not been clearly identified, it may be the pore filling secondary phase observed on the Nd-britholite powders recovered after the open-system experiments performed in basic solutions (see Fig. 2(c)).

5.2. Estimation of Nd-britholite solubility constants

One of the original goals of this study was to constrain the solubility of Nd-britholite to allow estimates of its stability in natural systems. This effort was hindered by a number of factors including difficulties in defining the solubility of a solid solution, the low concentration of Nd in the reactive fluids, and the precipitation of secondary phases. As such, the best estimate of Nd-britholite solubility constants, consistent with reaction (1), obtained in the present study was obtained from the measured Ca, P, Si, and pH of the final steady-state reactive solutions of the three closed-system experiments using Eq. (2). Owing to detection limitations, the value of Nd required for this calculation was obtained by assuming these reactive fluids were in equilibrium with Nd-rhabdophane. Resulting estimates of Nd-britholite solubility constants from the three closed-system experiments with an initial pH of 3, 4, and 5 are −91, −79, and −78, respectively. The reason for this scatter is unclear. It should nevertheless be emphasized that these values are estimated based on the assumption that the reactive solution at steady state in the closed-system experiments were indeed in equilibrium with the dissolving Nd-britholite and that these solutions were in equilibrium with Nd-rhabdophane. It was not possible to rigorously test these two assumptions in the present study.

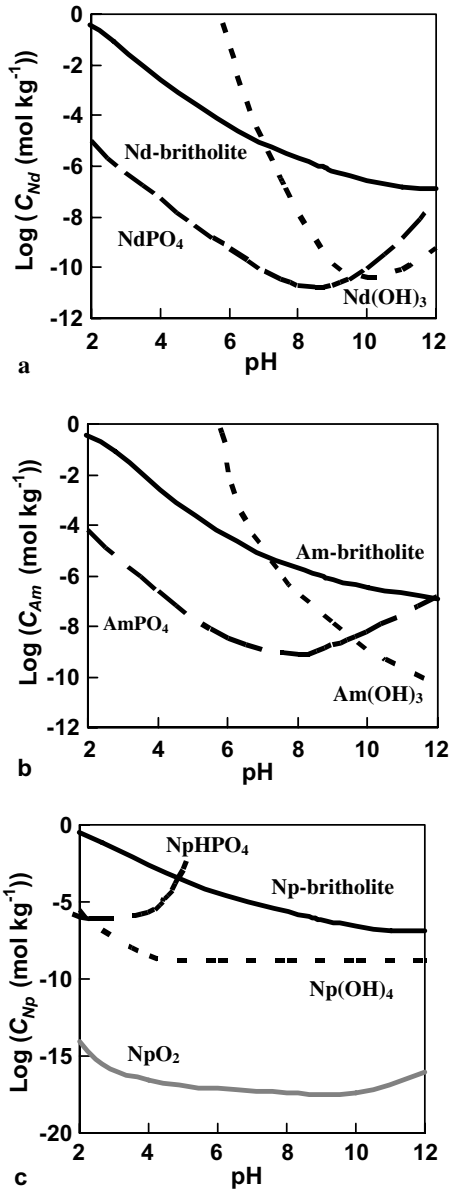

Fig. 8. Concentrations as a function of pH of (a) Nd in equilibrium with either Nd-britholite, Nd-phosphate, or $Nd(OH)_3$(c), (b) Am in equilibrium with either Am-britholite, Am-phosphate, or $Am(OH)_3$(c), and (c) Np in equilibrium with either Np-britholite, NpO_2, or $Np(OH)_4$(c). The equilibrium constant for all britholite dissolution reactions was taken to be −79 (see text). Concentrations of Nd, Am, and Np in equilibrium with phosphate bearing phases was computed assuming the solution had the same metal/P and metal/Ca ratio as the equilibrium phase.

5.3. Implications for radioactive actinide storage

Nd-britholite dissolved in the experiments described above provoked the precipitation of the Nd-rhabdophane and possibly $Nd(OH)_3$(c) as the reactive fluid became supersaturated with respect to these secondary phases. This also appears likely to be the case in natural systems. For example, the concentrations of Nd in equilibrium with Nd-britholite are compared with those in equilibrium with Nd-rhabdophane and $Nd(OH)_3$(c) in Fig. 8(a). The results shown in this figure suggests that neodymium concentrations will be influenced by the precipitation of secondary phosphates to pH 11 and of $Nd(OH)_3$(c) at higher pH. Although it is unlikely that the precipitate forms a protective layer due to the differing structures of the dissolving and precipitating phases [42], the formation of secondary Nd-rich phases may limit strongly aqueous neodymium concentrations coexisting with Nd-britholite in natural systems.

To assess if similar secondary phases may influence the concentration of radioactive actinides coexisting with analogous actinide–britholite phases, the concentration of Am and Np in equilibrium with Am-britholite or Np-britholite are compared with those in equilibrium with phosphate, hydroxide, and oxide phases in Fig. 8(b) and (c). Due to the lack of thermodynamic data, the equilibrium constants for Am-britholite and Np-britholite were assumed to be equal to that of Nd-britholite. For the case of americium, the secondary phosphate phases ($AmPO_4$ or $AmPO_4 \cdot nH_2O$) are estimated to be more stable than Am-britholite at <pH 10 whereas $Am(OH)_3$ is estimated to be more stable at higher pH. These calculations are supported by the observation of americium phosphate precipitation on dissolving borosilicate glass [43], monazite [36], and americium–thorium phosphate diphosphate solid solutions [34]. Similarly, secondary oxide and hydroxide Np phases are computed to be more stable than Np-britholite at all pH.

6. Conclusions

Nd-britholite dissolution rates are found to decrease with increasing pH from 2 to 7 but to be constant at pH > 8, consistent with $r_{Ca} = 10^{-6.5} a_{H^+}^{0.5} + 10^{-10.4}$mol/m^{2}s. As such this material will be most resistant to corrosion at the alkaline conditions that may be present at waste storage sites. Dissolution was also accompanied by the precipitation of Nd-rhabdophane, which further limits the mobility of Nd during Nd-britholite dissolution. By analogy, it seems likely that actinide-bearing britholites will be equally resistant to corrosion and provoke

actinide-rich secondary phase formation during their dissolution in alkaline solutions. This suggests that britholite possess several advantages for the immobilization of actinides in waste storage sites.

Acknowledgements

The authors wish to thank Christophe Guy, Christelle Latrille, Oleg Pokrovsky, Jean-Louis Dandurand, Jean-Marc Montel, Najatte Harouiya, Stephan Köhler, Cyril Coppel, and Lionel Campayo for insightful discussions during this study. We greatly appreciate the valuable technical assistance from Jocelyne Escalier, Carole Boucayrand, Stephanie Levet and Alain Castillo.

References

[1] K. Horie, H. Hidaka, F. Gauthier-Lafaye, Geochim. Cosmochim. Acta 68 (2004) 115.
[2] J. Carpena, in: P. Van den Haute, F. de Corte (Eds.), Advances in Fission Track Geochronology, Kluwer Academic, Dordrecht, 1998, p. 81.
[3] J. Chaumont, S. Soulet, J.C. Krupa, J. Carpena, J. Nucl. Mater. 301 (2002) 122.
[4] S. Soulet, J. Carpena, J. Chaumont, O. Kaitasov, M.O. Ruault, J.C. Krupa, Nucl. Instrum. Meth. Phys. Res., Sect. B (Beam Interact. Mater. Atoms) 184 (2001) 383.
[5] F. Ben Ayeda, J. Bouaziza, I. Khattechb, K. Bouzouita, Annales de Chimie Science des Matériaux 26 (2001) 75.
[6] M. Bertholus, M. Defranceschi, Les apatites: des phosphates naturels, in: Techniques de l'ingénieur, 2004, AF 6610.
[7] C. Guy, F. Audubert, J.-E. Lartigue, C. Latrille, T. Advocat, C. Fillet, C.R. Phys. 3 (2002) 827.
[8] L. Boyer, J. Carpena, J.L. Lacout, Solid State Ion. 95 (1997) 121.
[9] R. El Ouenzerfi, C. Goutaudier, M.Th. Cohen-Adad, G. Panczer, G. Boulon, J. Lumin. 102&103 (2003) 426.
[10] M. Higuchi, K. Kodaira, S. Nakayama, J. Cryst. Growth 207 (1999) 298.
[11] J. Carpéna, L. Boyer, M. Fialin, J.-R. Kiénast, J.-L. Lacout, C.R. Earth Planet. Sci. 333 (2001) 373.
[12] M. Higuchi, H. Katase, K. Kodaira, S. Nakayama, J. Cryst. Growth 218 (2000) 282.
[13] R. El Ouenzerfi, M.-T. Cohen-Adad, C. Goutaudier, G. Panczer, Solid State Ion. 176 (2005) 225.
[14] N. Dacheux, N. Clavier, A.-C. Robisson, O. Terra, F. Audubert, J.-E. Lartigue, C. Guy, C.R. Chimie 7 (2004) 1141.
[15] N.A. Chapman, J.A.T. Smellie, Chem. Geol. 55 (1986) 167.
[16] K.B. Krauskopf, Chem. Geol. 55 (1986) 323.
[17] D. Langmuir, Aqueous Environmental Geochemistry, Prentice-Hall, New York, 1996.
[18] S. Nakayama, M. Higuchi, K. Kodaira, M. Sato, S. Kakita, T. Suzukie, K. Itohe, J. Eur. Ceram. Soc. 19 (1999) 507.
[19] Y. Masubuchi, M. Higuchi, K. Kodaira, J. Cryst. Growth 247 (2003) 207.
[20] M. Higuchi, K. Kodaira, S. Nakayama, J. Cryst. Growth 216 (2000) 317.
[21] L. Boyer, Synthèse et caractérisations d'apatites phosphosilicatées aux terres rares: application au nucléaire, PhD thesis, Toulouse, France, 1998.
[22] D.C. Thorstenson, L.N. Plummer, Am. J. Sci. 277 (1977) 1203.
[23] M. Rabinowicz, J.-L. Dandurand, M. Jakubowski, J. Schott, J.P. Cassan, Earth Planet. Sci. Lett. 74 (1985) 387.
[24] A.C. Lasaga, Rev. Miner. 8 (1981) 135.
[25] P. Aagaard, H.C. Helgeson, Am. J. Sci. 282 (1982) 237.
[26] E.H. Oelkers, J. Schott, J.-L. Devidal, Geochim. Cosmochim. Acta 58 (1994) 2011.
[27] E.H. Oelkers, Geochim. Cosmochim. Acta 65 (2001) 3703.
[28] S.J. Kölher, N. Harouiya, C. Chaïrat, E.H. Oelkers, Chem. Geol. 222 (2005) 168.
[29] J. Johnson, G. Anderson, D. Parkhurst, 2000 Database from 'thermo.com.V8.R6.230' prepared by at Lawrence Livermore National Laboratory (Revision: 1.11).
[30] A.J. Koppi, R. Edis, D.J. Field, H.R. Geering, D.A. Klessa, D.J.H. Cockayne, Geochim. Cosmochim. Acta 60 (1996) 1695.
[31] J.F. Banfield, R.A. Eggleton, Clays Miner. 37 (1989) 113.
[32] J.-J. Braun, J. Viers, B. Dupré, M. Polvé, J. Ndam, J.-P. Muller, Geochim. Cosmochim. Acta 62 (1998) 273.
[33] W.N. Sawka, J.F. Banfield, B.W. Chappell, Geochim. Cosmochim. Acta 50 (1986) 171.
[34] A.E. Taunton, S.A. Welch, J.F. Banfield, Chem. Geol. 169 (2000) 371.
[35] A.E. Taunton, S.A. Welch, J.F. Banfield, J. Alloys Compds. 303&304 (2000) 30.
[36] A.C. Robinson, N. Dacheux, J. Aupiais, J. Nucl. Mater. 306 (2002) 134.
[37] E.C. Buck, J.K. Bates, Appl. Geochem. 14 (1999) 635.
[38] F. Poitrasson, E.H. Oelkers, J. Schott, J.-M. Montel, Geochim. Cosmochim. Acta 68 (2004) 2207.
[39] N. Clavier, Elaboration de phosphate–diphosphate de thorium et d'uranium (β-PDTU) et de matériaux composites β-PDTU/Monazite à partir de précurseurs cristallisé-Etude du frittage et de la durabilité chimique, PhD thesis, Paris XI, France, 2004.
[40] H. Guan, Y. Zhang, J. Solid State Chem. 177 (2004) 781.
[41] X. Liu, R.H. Byrne, Geochim. Cosmochim. Acta 61 (1997) 1625.
[42] P. Cubillas, S. Köhler, M. Prieto, C. Causserand, E.H. Oelkers, Geochim. Cosmochim. Acta 69 (2005) 5459.
[43] W.L. Ebert, J.K. Bates, W.L. Bourcier, Waste Manage. 11 (1991) 205.
[44] C. Chaïrat, E.H. Oelkers, J. Schott, J.-E. Lartigue, Geochim. Cosmochim. Acta 68 (2004) A145.